# Contact mechanics of open-cell foams with macroscopic asperities

Alexandre Wilkinson, Jean-Philippe Crété, Stéphane Job, Mohamed Rachik, Nicolas Dauchez

▶ **To cite this version:**

Alexandre Wilkinson, Jean-Philippe Crété, Stéphane Job, Mohamed Rachik, Nicolas Dauchez. Contact mechanics of open-cell foams with macroscopic asperities. 2024. hal-04502703

**HAL Id: hal-04502703**
**https://hal.science/hal-04502703**

Preprint submitted on 13 Mar 2024

**HAL** is a multi-disciplinary open access archive for the deposit and dissemination of scientific research documents, whether they are published or not. The documents may come from teaching and research institutions in France or abroad, or from public or private research centers.

L'archive ouverte pluridisciplinaire **HAL**, est destinée au dépôt et à la diffusion de documents scientifiques de niveau recherche, publiés ou non, émanant des établissements d'enseignement et de recherche français ou étrangers, des laboratoires publics ou privés.

Distributed under a Creative Commons Attribution - NonCommercial - NoDerivatives 4.0 International License

# Contact mechanics of open-cell foams with macroscopic asperities

A. Wilkinson[a], J.-P. Crété[b], S. Job[b], M. Rachik[a], N. Dauchez[a]

[a] *Université de technologie de Compiègne, laboratoire Roberval, Centre de recherche Royallieu - CS 60 319 - 60 203 Compiègne Cedex, France.*

[b] *Laboratoire Quartz (EA-7393), Institut Supérieur de Mécanique de Paris (ISAE-Supméca), 93400 Saint-Ouen-sur-Seine, France.*

**Abstract**

Poroelastic materials mounted against rigid surfaces often result in partial contact between the two, affecting their mechanical interaction. The surface roughness of cellular materials introduces complexity in predicting their behavior due to the interface with partial contact. This interface exhibits a stiffness distinct from the bulk material, which is driven by the surface asperities and the preload. This study conducts compression experiments on an open-cell poroelastic melamine foam, and compares them to finite elements simulations and analytic predictions. The material's intrinsic stress-strain nonlinearity is accounted for, and an original hyperelastic aging model is proposed to achieve accurate predictions of its compression stiffness across multiple time scales. Predicting the compression stiffness of a macroscopic pyramidal asperity demonstrates a good agreement with the simple analytic solution for an elastic pyramidal geometry. Using a Greenwood-Williamson-like model based on the distribution of asperities of different heights, we propose a method to predict the contact stiffness of a rough surface. Our findings have important implications for understanding and optimizing efficient vibration barriers, resulting from the simple stacking of layers and screens of raw poroelastic materials, a configuration widely adopted in the transportation and civil engineering industries.

*Keywords:* contact stiffness, poroelastic material, open-cell foam, viscoelasticity, relaxation, hyperelasticity, Kelvin cells, pyramidal asperity, Greenwood-Williamson model

*Email address:* alexandre.wilkinson@utc.fr (A. Wilkinson)

## 1. Introduction

Poroelastic materials have many practical applications thanks to their high porosity, flexibility, and damping. Notably, polymer foams are used for shock absorption in packaging (Wang and Low, 2005; Ge and Rice, 2018), impact damping (Oh et al., 2020; Belingardi et al., 2001), sometimes associated with a structure (Yang et al., 2021; Lee et al., 2022). As components of multilayer panels, they contribute significantly to vibration reduction (Chen and Sun, 2012) and acoustic insulation (Novak, 1992; Bolton et al., 1996; Panneton and Atalla, 1996; Lagarrigue et al., 2013; Luo and Huang, 2014). Porous screens are also used to provide radiation attenuation of vibroacoustic sources (Amédin et al., 1995; Cummings et al., 1999; Doutres et al., 2007; Campolina et al., 2012), as for the encapsulation of car combustion engines (Lei, 2018). In all of these use cases, accurately modeling the porous layer behavior usually requires a thorough understanding of its mechanical response, which can be difficult to predict for several reasons.

The first obstacle relies on the difficulty of interpreting the stiffness characterization of these materials. A round-robin study on their dynamic mechanical characterization revealed that the measured mechanical properties can span several orders of magnitude, depending on the laboratory and the method used (Bonfiglio et al., 2018). Moreover, material characterization without preload is often sought, but there is no widely accepted procedure to do so in practice. Some authors (Dauchez, 2014; Chevillotte et al., 2020) suggest extrapolating these properties from measurements at different compression amounts, but this method can be difficult to implement because of material nonlinearity and the difficulty of identifying the stress-free position when the sample has an uneven or non-flat surface.

A second difficulty comes from predicting the mechanical behavior of porous materials *in-situ* when installed against rigid walls. The inherently irregular surface of porous materials results in partial contact and heterogeneous a preload, which affect their mechanical behavior. Understanding the mechanical stiffness of a porous material, especially at its contact boundary, is therefore crucial in predicting its *in-situ* behavior in many situations. Guastavino and Göransson (2007) observe a soft boundary layer at the contact boundaries of foam samples using 3D image correlation. Dauchez et al. (2002) theorize that such a zone is caused by damaged cells at the surface of the sample when it is cut into shape. Mao et al. (2021) model this phenomenon by damaging the struts of the cells composing the material near the sample's boundaries by disconnecting their extremities, to mimic the damage experienced by the material sample when it is cut. This method, however,

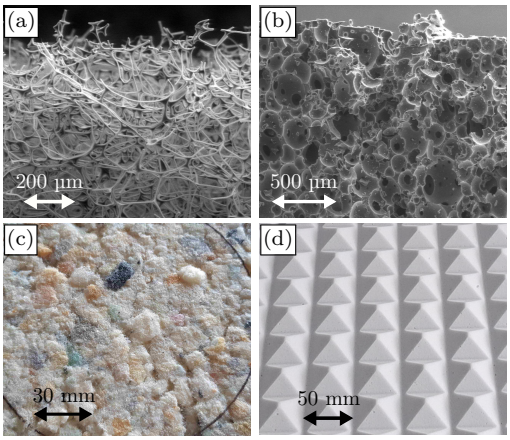


Figure 1: Examples of uneven porous material surfaces, due to (a) uneven cutting on an open-cell material (microscopic scale), (b) uneven cutting on a closed-cell material (microscopic scale), (c) industrial manufacturing process (mesoscopic scale) and (d) intentional design for acoustic absorption and aesthetic purposes (macroscopic scale).

does not account for material surface roughness. This surface roughness of raw poroelastic layers can lie at different length scales, and, for example, can result from uneven cutting (Figure 1(a) and Figure 1(b)), manufacturing processes (Figure 1(c)) or intentional design (Figure 1(d)).

To improve the modeling of compressed porous materials against a surface by accounting for their irregular surface shape, three phenomena should be accounted for. First, porous materials made of cellular structures are known to exhibit a nonlinear behavior as they are compressed. This is historically well documented (Ashby, 1983; Gibson, 1989; Gibson and Ashby F, 1997; Dauchez et al., 2002; Gong et al., 2005; Jaouen et al., 2008; Geslain et al., 2011; Schiffer et al., 2018) and can be modeled using a nonlinear constitutive behavior model, such as a hyperelastic model (Mooney, 1940; R.S.Rivlin, 1947; Rivlin et al., 1951). Second, porous materials undergo stress relaxation over time while under constant strain, similarly to viscoelastic materials, leading to a significant stress deviation over long durations. Third, the surface roughness can be modeled using a statistical surface roughness approach. The multi-asperity surface roughness model proposed by Greenwood and Williamson (Greenwood and Williamson, 1966; Greenwood and Tripp, 1967) amounts to representing a rough surface by a sum of asperities of known stiffness following a height probability distribution. This requires that the surface's asperities be considered homogeneous, a condition which Hentati et al. (2020) have shown to be valid for a cellular material that has enough strands in contact with the rigid indenting plane.

The aim of this study is thus to predict the compression stiffness of macroscopic asperities of a rough open-cell material's surface, by accounting for material nonlinearity, relaxation, and asperity geometry.

This article is structured as follows. In Section 2, the material's nonlinearity and relaxation are studied to establish its constitutive laws. This characterization is performed on a homogeneous cylinder of melamine. Then, in Section 3, the prediction of the stiffness of a single pyramidal asperity of melamine foam is performed analytically and numerically and compared with experimental results. Square-base pyramidal asperities are considered because they allow for accurate control over their geometry in their manufacturing process. Compression ramps are performed, in which the ramp response of the material is examined, and isolated surface asperities are studied in order to disregard the transition to the bulk material behavior below the asperities. Finally, in Section 4, a surface of multiple pyramidal asperities of different heights is created and compared with predictions to assess the validity of their integration within a surface roughness model.

## 2. Material nonlinearity and relaxation

In this section, the material's constitutive behavior is examined and modeled. A compression ramp is applied to a cylindrical sample of the studied material to obtain a force-displacement curve, which is turned into a stress-strain relationship to express its constitutive behavior.

### *2.1. Experimental setup*

Compression measurements are performed on an Anton Paar MCR 502 rheometer. Cylindrical foam samples are placed between two plates, as pictured in Figure 2. The top plate compresses the sample, up to around 80 % of its initial height $H_0 = 19.3$ mm. The top plate's position relative to the bottom plate and the compression force are measured over time. The temperature is also tracked to ensure its stability. The cylindrical sample is taped to the plate so that all the cells at the interface (about 42 000 cells within the 29 mm in diameter cross-section) are in contact with it. Taping the sample rules out effect of surface irregularities, allowing interpreting the deformation of the sample as an effect of its bulk properties only, and avoids any contact detection protocol to determine the reference deformation.

### *2.2. Material hyperelasticity*

The schematic of the uniaxial compression is presented in Figure 2(b). Nominal stress and strain expressions are used, and strains are supposed uniform during the tests. The axial strain is expressed as $\varepsilon = \frac{\delta}{H_0}$, where $\delta$ is the compression distance, and the axial stress is expressed as $T_L = \frac{F}{S_0}$, where F is the measured compression force and $S_0$ is the initial sample cross-section

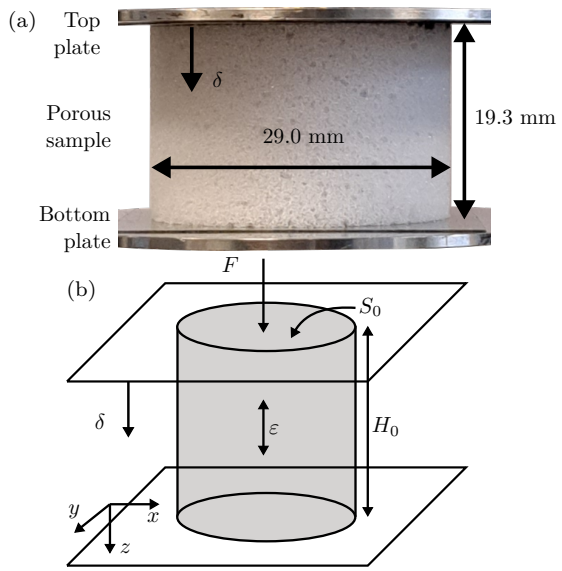


Figure 2: Experimental setup to measure the compression force and the compression distance over time. (a) Experimental cylindrical melamine foam sample between the two plates of the rheometer. (b) Schematic of a cylindrical sample being compressed uniaxially.

area. Measurement results averaged over five cylindrical samples are shown in Figure 3 reveal the nonlinearity between stress and strain. The three usual compression regimes can be identified: the quasi-linear bending of the surface strands between 0 % and 2 % strain, the buckling of the cell walls between 2 % and 20 % strain, and the densification of the cell struts which begins above 20 % strain. The strain in the bulk of the foam is thus inhomogeneous by nature, including at the scale of the finite size of the constituting cells. It is thus worth noting that defining an elastic modulus from the stress-strain relation relies on an effective feature at the scale of the sample itself, rather than a definition stemming from homogenization techniques.

The tangent modulus of the material $E_{tan}$ is defined as the slope of the stress-strain curve at a given position, and is obtained as $E_{tan} = \frac{\partial T_L}{\partial \varepsilon}$. The secant modulus $E_{sec}$ is defined as the ratio of the stress $T_L$ over the strain $\varepsilon$: $E_{sec} = \frac{T_L}{\varepsilon}$. The secant modulus $E_{sec}$ is different from the tangent modulus $E_{tan}$, as shown in Figure 3(b). Indeed, between 0 % and 20 % strain, the tangent modulus $E_{tan}$ decreases from 290 kPa to 12 kPa due to cell buckling. It then increases to 35 kPa at 50 % strain and 436 kPa at 80 % strain due to cell densification. Meanwhile, the secant modulus $E_{sec}$ drops from 290 kPa for strains less than 1 % to 50 kPa at 25 % strain and 34.7 kPa at 50 % strain, as a consequence of buckling. Then, it increases to 72 kPa at 80 % strain due to densification.

Additionally, the secant modulus at the inflection point $I$, $E_I = E_{sec}(\varepsilon_I)$, is computed at $\varepsilon_I = 20$ % strain. This corresponds to the minimum of the tangent modulus $E_{tan}$, and marks the

transition from buckling to the start of densification. This inflection point is sometimes called the crush strain in the literature (Tan et al., 2002; Li et al., 2006; Xing et al., 2023). $E_I$ has a value of 58.0 kPa and will be used as an average equivalent modulus for the material in Section 3.5.3. It is worth noting that the tangent modulus $E_{tan}$ is obtained here from a compression ramp, which can give different values from the dynamic tangent modulus, as shown by some authors (Cavender and Kinkelaar, 1996; White et al., 2000) and found by some of our measurements not presented here.

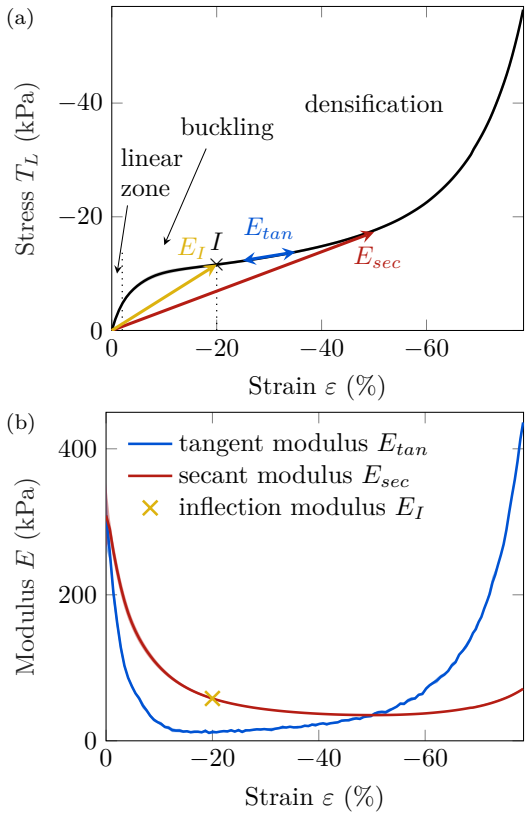


Figure 3: (a) Nonlinear stress-strain relationship of compressed foam averaged over five measurements. (b) Tangent modulus $E_{tan}$ and secant modulus $E_{sec}$ as a function of strain, and inflection modulus $E_I$ location.

The nonlinear behavior of the material can be predicted with a hyperelastic model that is tailored for polymer foams subject to large strains (Abaqus Inc., 2006b; Hill, 1979; Storåkers, 1986). This model is called the hyperfoam model in Abaqus and is derived from Ogden's hyperelastic model (Ogden, 1972). It relates the stress and strain in the uniaxial mode through

$$T_L = \frac{2}{\lambda} \sum_{i=1}^{N} \frac{\mu_i}{\alpha_i} (\lambda^{\alpha_i} - J^{-\alpha_i \beta_i}), \tag{1}$$

where $N$ represents the number of terms of the model, $\beta_i = \frac{\nu_i}{1-2\nu_i}$ with $\nu_i$ the $i$th Poisson ratio,

Table 1: Parameter values obtained for the hyperfoam model, with their standard deviation. These parameters are obtained from the instantaneous stress-strain relationship of a compressed cylindrical sample of melamine foam.

| $\alpha_1$ (-) | $\mu_1$ (kPa) | $\nu_1$ (-) |
|---|---|---|
| 49.8 | 189.1 | 0.005 |
| $\pm$ 8.2 | $\pm$ 28.3 | $\pm$ 0.002 |

$\lambda = 1 + \varepsilon$ the stretch in the compression direction, and $J$ the elastic volume ratio. Increasing the number of terms $N$ in the hyperfoam model can help improve the fit over the measured data range. However, it also increases the risk of violating the Drucker stability condition for different strain values and strain modes, such as uniaxial, equibiaxial, shear or volumetric strains (Abaqus Inc., 2006a). Since only uniaxial compression is studied here, $N = 1$ is reliable. For uniaxial strain and assuming a linear relationship between axial and lateral displacement, $J = \lambda(1 - \nu\varepsilon_1)^2$. This model therefore requires three parameters ($\alpha_1$, $\mu_1$, $\nu_1$) that can be fitted to measurements to represent the material's nonlinear stress and strain relationship. Their values computed from a 26 second-long compression ramp from 0 % to 80 % strain are given in Table 1.

### *2.3. Material relaxation*

When compression measurements are performed for different strain rates, a variation in the measured stress can be observed. This is shown in Figure 4, in which cylindrical samples were compressed experimentally for strain rates going from 3.0 $\%\,\mathrm{s}^{-1}$ to $3.7 \times 10^{-3}$ $\%\,\mathrm{s}^{-1}$. This corresponds to compression ramps lasting between approximately 26 s and 6 hours (or 21 600 s). The variation in the results can be explained by the viscous relaxation of the material. Standard protocols to measure the compression stiffness of rubber (ASTM International, 2001), flexible cellular materials ASTM International (2002), and certain foams in the industry (Renault, 2014) define a sequence of compressions and decompression cycles before taking measurements, resulting in values that incorporate the material's hysteresis.

In contrast, our interest lies obtaining material properties which are independent of its loading history. If measurements are performed quickly enough, the instantaneous time response of the material can be captured and its relaxation can be neglected. This is ideal because it is impractical to measure the long-term response of the material due to very long wait times. The experimental results reveal that for compression ramps short than 106 s, the stress-strain curves are very similar, indicating that they are representative of the material's instantaneous response. It is concluded that the material's instantaneous response can be obtained when it is excited quickly enough,

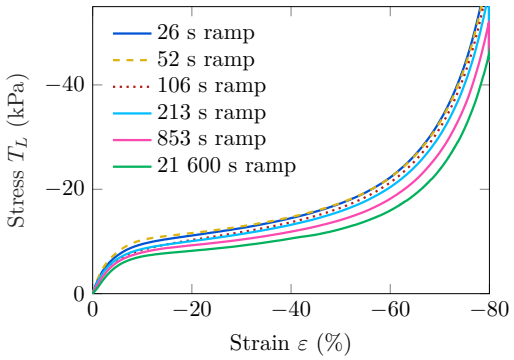


Figure 4: Experimental stress-strain results for cylindrical melamine samples compressed from 0 % strain to 80 % strain at different strain rates, resulting in ramps of different durations.

that is to say for strain rates greater than 1.5 $\%\,\mathrm{s}^{-1}$. This hypothesis is verified with an original hyperelastic aging model in Appendix A.

## 3. Compression stiffness of a single pyramidal asperity

The behavior of a single pyramidal asperity is analyzed in this section. First, the open-cell microstructure of the porous material is modeled and compared with the expected results for a continuous medium. Then, the material hyperelasticity is integrated with the pyramidal geometries to shed light on the interaction between the shape and the material nonlinearities.

### *3.1. Experimental setup*

The same compression measurement setup is used as for the cylindrical samples described in Section 2.1. Compression ramps are performed quickly enough, such that the strain rate is greater than 1.5 $\%\,\mathrm{s}^{-1}$ and the instantaneous stress response can be measured. Square-base pyramidal asperities of melamine foam, with a side angle of $\theta = 45°$ from the horizontal plane, are created to obtain the relation between their compression force and compression distance. The geometry of the pyramids is presented in Figure 5(a) and a real pyramid of melamine foam is pictured in Figure 5(b). Five repetitions are performed on different pyramids to obtain an average result with a standard deviation.

The pyramid tips are supposed to be pointy, however due to imperfections in the cutting process and the microstructure of the material, there is an uncertainty on the tip width $a_0$ in the same order of magnitude as the foam's cell size $h_0$ and ligament size $l_0$: $a_0 \sim h_0 \sim l_0$. Since this bias is at the edge of a continuous description of the pyramids, it is assumed to have a negligible effect at the macroscopic scale, such that $a_0 = 0$. The cell size $h_0$ for melamine foam is found

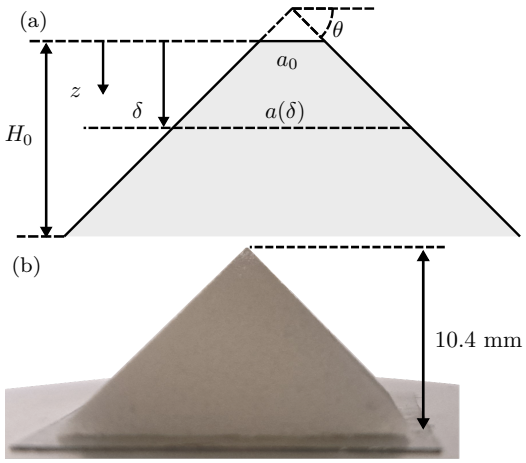


Figure 5: (a) Diagram of a pyramid being compressed by an amount $\delta$. The flat top of the pyramid of length $a_0$ is due to possible cutting defects and microstructural cell size. (b) Picture of a pyramid created experimentally.

between 0.10 mm and 0.15 mm by Kino and Ueno (2008), and between 0.1 mm and 0.2 mm by Hentati et al. (2020), both estimations being obtained from independent scanning electron microscopy measurements. In the frame of our study, we chose $h_0 = 0.125$ mm as a fair value lying in both intervals, to identify the effects related to the cell size of melamine foam in dimensionless quantities.

### *3.2. Numerical analysis: open-cell microstructural model*

A Finite Elements Method (FEM) model is created to accurately represent the 3D stress and strain undergone by a compressed open-cell pyramidal sample made from an open-cell material. This model represents the microstructure of the porous network using Kelvin cells. It attempts to capture the nonlinear phenomena of the material through its microgeometry, such as the initial contacts with an indenting plate, involving the progressive recruitment of a finite number of free ligaments and struts near the foam's surface, and their buckling at large strains.

The open-cell microstructure is modeled using distorted Kelvin cells composed of beam element, using the same modeling approach as Hentati et al. (2020). Material parameters and cell properties are presented in Table 2. The cell height is the same as the M7 polyurethane foam in reference (Doutres et al., 2011) and the strut length and radius are from references (Tan Hoang and Perrot, 2012; Hoang, 2012). The aim of this numerical model is to be qualitative. Consequently, its specifications (cell size, elasticity) describe a typical open-cell foam but do not match the melamine foam used in this study quantitatively, and the results are examined as dimensionless relative to the cell size. Matching quantitatively the parameters of this model to the specifications

Table 2: Parameters used in the microstructural Kelvin cell FEM model.

| | | |
|---|---|---|
| Avg. cell height | $h_0$ | 0.574 mm |
| Avg. beam length | $l_0$ | 0.203 mm |
| Beam radius | $r_0$ | 0.021 mm |
| Elastic modulus | $E$ | 3000 MPa |
| Poisson ratio | $\nu$ | 0.38 |
| Mass density | $\rho$ | 1300 kg.m$^{-3}$ |
| Mass damping | $\alpha_R$ | 0 |
| Stiffness damping | $\beta_R$ | $1.10^{-4}$ |

of the sample is a matter of adjusting a prefactor, it thus brings less understanding than analyzing the trends qualitatively.

Rayleigh damping $(\alpha_R,\, \beta_R) = (0,\, \tau_R)$ is introduced in the beams' response to improve computation convergence. A viscous relaxation time, $\tau_R = 10^{-4}$ s, relying on the beam material is imparted by adding a viscous-like damping stress tensor $\boldsymbol{\sigma_d} = \tau_R \boldsymbol{D}\dot{\boldsymbol{\varepsilon}}$ to the elastic tensor, with $\dot{\boldsymbol{\varepsilon}}$ the strain rate tensor and $\boldsymbol{D}$ the elastic constitutive tensor. The value of $\tau_R$ is chosen much smaller than the loading duration of the sample ($\tau_L > 10$ s), such that the damping has no other effect than accelerating the numerical convergence, by filtering spurious and non-physical high-frequency artifacts (*e.g.* when light and stiff submillimetric edge ligaments go into resonance).

The pyramidal shape is created by intersecting a wide parallelepipedic lattice of Kelvin cells with a pyramidal geometry of total height $H_0 = 10.0$ mm and of side angle $\theta = 50°$ using a Python routine. An angle $\theta = 50°$ is used, instead of the 45° considered in experiments, in order to break up the geometric repetition stemming from the Kelvin cells along the side of the pyramid at 45°. The resulting pyramid of Kelvin cells is compressed by a rigid plate by an amount $\delta = 5$ mm. A vertical slice of the 3D Kelvin cell pyramid is shown in Figure 6(a).

The frictionless contact between the cell struts and the rigid plane is handled by Abaqus. Only a quarter of the pyramid is created by exploiting the symmetry of the geometry and of the loading. Each strut is composed of two aligned B32 beam elements. A uniformly distributed random displacement, ranging within ±7.5 % of the strut lengths, *i.e.* ±15.2 µm, is applied to each node's position. No contact between beams is considered, meaning that the densification of the material at large strains can not be represented. An implicit numerical time integration scheme is used.

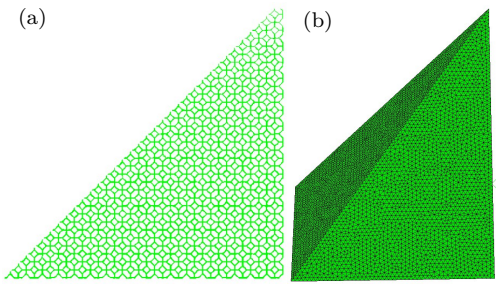


Figure 6: Numerical model meshes of the material geometry. Quarter-pyramids are modeled by exploiting the problem's symmetry. (a) Slice of the FEM model composed of approximately 1 185 Kelvin cells. (b) Model with continuous elements composed of approximately 353 553 elements.

### *3.3. Analytic model for a compressed pyramidal asperity*

The expected tendency of the compression force of a compressed pyramid can be approximated using geometric considerations. Using geometric arguments only, Hooke's law states that the pyramid's compression force $F$ per unit of contact area $S(\delta)$ is proportional to an elastic modulus $E$ and the strain $\varepsilon(\delta)$:

$$\frac{F(\delta)}{S(\delta)} \propto E\varepsilon(\delta). \tag{2}$$

The cross-section area $S(\delta)$ of the pyramid at compression distance $\delta$ is computed as

$$S(\delta) = a^2(\delta), \tag{3}$$

where $a(\delta)$ is the length of the sides of a horizontal cross-section of the pyramid :

$$a(\delta) = a_0 + \frac{2\delta}{\tan(\theta)}, \tag{4}$$

where $a_0$ is neglected in our case. Therefore, combining Equation 2 to Equation 4 provides a tendency of the compression force for the pyramid as

$$F \propto \frac{E}{\tan\theta}\delta^2. \tag{5}$$

In this case, the force $F$ increases quadratically with the compression distance $\delta$, which confirms findings by several authors that pyramidal indenters behave similarly to cones in contact mechanics, which also behave as $F \propto \delta^2$, up to a small correction factor (Antunes et al., 2006; King, 1987). Interestingly, the naive geometric model provided in Equation 5 agrees with the exact prediction of the compression force $F$ of a pyramid being indented by a rigid plane by an amount $\delta$ (Sirghi

et al., 2008; Sneddon, 1965)

$$F = \frac{4}{\pi\sqrt{\pi}} \frac{E^*}{\tan\theta} \delta^2, \tag{6}$$

where $E^* = \frac{E}{(1-\nu^2)}$ is the effective elastic modulus of the material and $\nu$ is its Poisson ratio. In other words, the resulting force is expected to evolve quadratically with the compression distance $\delta$, and its magnitude is driven by a prefactor $\frac{E}{\tan\theta}$ which is proportional to the equivalent material modulus $E$ and inversely proportional to the pyramid angle tangent $\tan\theta$.

### *3.4. Comparison between predictions and measurements*

In this section, the results for the measurements, the analytic prediction from Equation 5, and the Kelvin cell numerical simulation are compared to each other in Figure 7. The compression distance $\delta$ is normalized by the cell height $h_0$, in order to compare the qualitative features of the numerical model with the experiment. The magnitude of the numerical predictions are not compared quantitatively to the experimental results because the numerical Kelvin cells are not quantitatively equal to the cells of the melamine foam; attention is focused on qualitative tendency. A key question is the validity of a continuum mechanics description in the context of an inherently inhomogeneous porous material made of finite-size cells.

The contact detection protocol to determine the accurate location of the tip of the undeformed pyramid is performed by translating the indenting plate by 0.1 mm increments until sensing at least a 0.01 N force, where 0.01 N is the reading threshold of the built-in sensor display. Then, extrapolating the force F - displacement $\delta$ relationship above 0.01 N with the behavior determined in Equation 5, $F \propto (\delta - \delta_0)^2$, allows determining the contact origin offset $\delta_0 \simeq 0.23$ mm, with an error likely bound well below the cell size. In any case, the error on the estimation of the offset causes a valuable relative correction, but which is insignificant in absolute values at small deformations. In turn, the offset correction and its uncertainty quickly become negligible at deformations larger than few cell sizes, due to the $F \propto (\delta - \delta_0)^2$ nature of the force.

As predicted analytically, both the measured pyramid and the numerical model forces seem to increase quadratically with the compression distance. Nonetheless, for small strains (*i.e.* $\delta/h_0 \approx 2$, or fewer than 20 cells in contact with the indenting plane), the experimental stress does not follow the expected quadratic tendency with the compression distance. A first explanation for this is the imperfectly cut tip of the pyramid, and a second is that the material cannot be considered as a continuous medium at the scale of the cell size. This corroborates previous results by Hentati

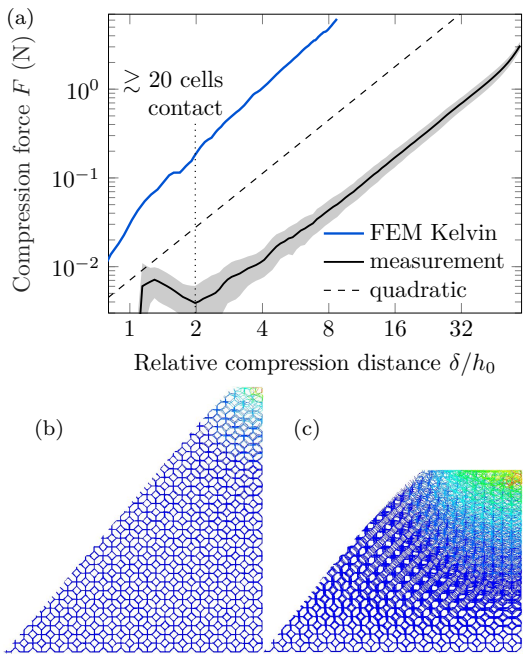


Figure 7: (a) Force and compression distance relationship for a single pyramid, obtained experimentally and with the Kelvin cell FEM model. The standard deviation measured over 5 repetitions is given. The expected quadratic tendency is plotted. The vertical line indicates the compression distance where the pyramid cross-section area is equal to the surface area of 20 cells. (b) Deformation of the Kelvin cell FEM pyramid at $\delta = 1$ mm, *i.e.* $\delta/h_0 = 1.7$ and approximately 15 cells in contact, and (c) $\delta = 4$ mm, *i.e.* $\delta/h_0 = 7.0$ and approximately 247 cells in contact.

et al. (2020) that material homogeneity is valid once enough material strands are in contact with the rigid indenting plane, which is a few tens of strands.

For large compression distances, around $\delta/h_0 \approx 50$, the measured force diverges from the expected quadratic tendency because the strain field inside the pyramid reaches the rigid plate below the pyramid. This phenomenon can be understood thanks to the numerical simulation: for small strains in Figure 7(b), the strain field does not extend much into the pyramid, whereas for larger strains in Figure 7(c), the strain field extends further and spherically into the pyramid, until it reaches the plate below the pyramid. This increases its apparent rigidity since the problem is not a single contact behavior anymore.

Finally, in a non-trivial way, the nonlinear hyperelasticity of the material does not appear in the experimental results in Figure 7. In the following section, the material nonlinearity is included in models of a pyramid to understand how it interacts with the shape nonlinearity.

### *3.5. Models accounting for non-homogeneous strain*

The objective of this section is to understand how the material nonlinearity and the shape nonlinearity interact by combining the hyperelastic model with the pyramidal geometry.

*3.5.1. Analytic slices model*

An analytic model accounting for varying strain and modulus throughout the height of the pyramid is investigated. This model consists in studying horizontal slices throughout the height of the pyramid, in which the strain is considered constant. Considering a constant force $F$ transmitted throughout the height of the pyramid, the local stress-strain relationship in a thin horizontal slice at distance $z$ from the pyramid tip gives

$$F = S(z)\, E_{sec}(\varepsilon(z))\, \varepsilon(z), \tag{7}$$

where $S(z)$ is the local cross-section area computed from Equation 3, and where the Poisson effect is neglected because the Poisson ratio was found small in Table 1. The strain $\varepsilon(z)$ in each horizontal slice is computed from Equation 7, and then the total compression distance $\delta$ is

$$\delta = \int_0^{H_0} \varepsilon(z) dz, \tag{8}$$

which yields the relationship between the force $F$ and the compression distance $\delta$.

Using this model, the strain throughout the height of the pyramid can be estimated for a given force $F$, as shown in Figure 8. Near the tip of the pyramid, where the contact area is small, the local strain is close to 100 %, meaning that the material is completely crushed: its contribution to the apparent stiffness disappears. Beyond this region, in the center of the pyramid, the strain and the modulus evolve quickly: this region mainly drives the relationship between applied force and the total compression distance of the pyramid. Near the base of the pyramid, the strain is closer to 0 %. In this zone, the pyramid has a high modulus and a high surface area: it hardly deforms and its contribution to the apparent stiffness is also small. The overall behavior is then mostly governed by pyramidal geometry, which leads to a $F \propto \delta^2$ law.

*3.5.2. Hyperelastic solid FEM model*

To obtain a more accurate 3D representation of the strain inside a pyramidal asperity, a pyramid made of a continuous solid hyperelastic material is simulated numerically under the same conditions. The model mesh is shown in Figure 6(b). Linear tetrahedral elements (C3D4) of average size 0.2 mm are used, ensuring results which are independent of the element size. The material behavior is described by a hyperfoam model using parameters from Table 1.

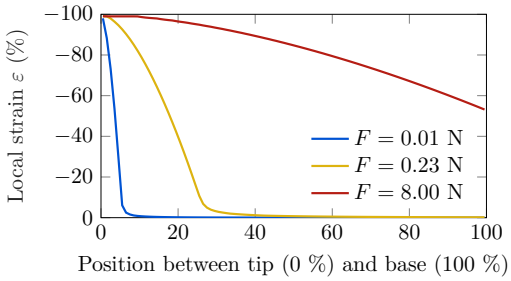


Figure 8: Strain throughout the height of the pyramid obtained from the analytic slices model for different values of applied compression force $F$.

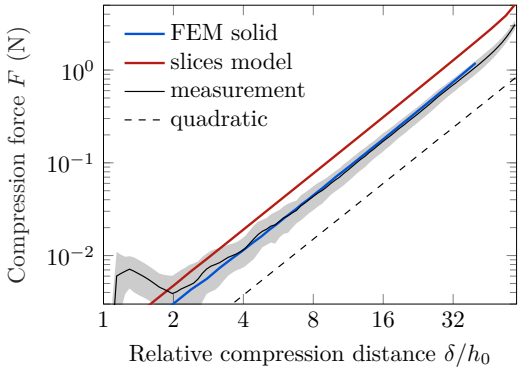


Figure 9: Compression force and compression distance relationship for the measured pyramid, the hyperelastic solid FEM model, and the analytic slices model. The expected quadratic tendency is also represented.

### *3.5.3. Results and interpretation*

The analytic slices model and the hyperelastic FEM model are compared to measurements in Figure 9. Both models follow the same tendency as a quadratic law, despite the hyperfoam material behavior used. The slices model overestimates the compression force, which could be due to the hypothesis of constant strain within each horizontal slice, since Figure 7(c) shows that the strain field front in fact extends spherically into the pyramid. The force predicted by the hyperelastic FEM model matches the quadratic tendency of the experiment accurately once the experimental compression distance provides a few tens of cells of contact, to bypass surface effects and the error on the height determination of the pyramids. Using Equation 6, the equivalent modulus fitted to the hyperelastic FEM results is $E = 65.3$ kPa and the modulus fitted to the experimental results is $E = 60.2$ kPa. These similar results validate the hyperfoam model in Table 1 for the pyramidal geometry. The constant prefactor modulus fitted to experimental results is chosen to represent the quadratic tendency of a single pyramidal asperity, by simplifying the strain-dependent modulus with an equivalent value, providing a reasonable prediction of experimental results within the whole range of probed deformations past the effect of the surface cells.

*3.5.4. Estimation of an equivalent modulus*

The aim of this section is to determine an appropriate constant modulus to approximate the hyperfoam law for the pyramid. Three hypotheses are proposed. A first option is to use the tangent modulus at small strains $E_{tan}(\varepsilon = 0) = 300$ kPa, as shown in Figure 3(b). This corresponds to the more classical definition of the linear elastic Young's modulus. A second option is to consider the pyramid as a sum of stiffnesses in series, in which case the overall stiffness is driven by the lowest stiffness. This means the overall stiffness can be approximated by the minimum of the secant modulus $E_{min} = \min(E_{sec}) = 35$ kPa, found for $\varepsilon = -50$ %. A third option is to consider the secant modulus at the inflection point $E_I = E_{sec}(I) = 58.0$ kPa, found for $\varepsilon = -20$ %, where the tangent modulus transitions from buckling to densification. This modulus serves as an average description of the material over its different compression regions, *i.e.* the first contacts, the linear, the buckling, and the densification zones.

The compression force of a pyramid using the slices model and the hyperfoam law $E_{sec}(\varepsilon)$ is shown in Figure 10. It is compared to models using the three proposed hypotheses $E_{tan}(\varepsilon = 0)$, $E_{min}$ and $E_I$. The small strain modulus $E_{tan}(\varepsilon = 0\ \%)$ overestimates the material stiffness, whereas the minimum of the secant modulus $E_{min}$ underestimates the material stiffness. Using the secant modulus at the inflection point $E_I$ gives a prediction that is close to the full strain-dependent secant modulus $E_{sec}(\varepsilon)$. Indeed, $E_I = 58.0$ kPa is a good approximation of the prefactor found by the FEM hyperelastic model $E = 65.3$ kPa for a pyramidal geometry in Figure 9.

In short, the constant modulus is largely surrounded by the tangent modulus at small strains $E_{tan}(\varepsilon = 0)$ and the minimum of the secant modulus caused by buckling $\min(E_{sec})$, but can be fairly well approximated by the secant buckling modulus $E_{sec}(I)$.

## 4. Application to a multi-asperity rough surface

After analyzing a single asperity, a rough surface of multiple asperities is now studied through a surface roughness model. The Greenwood-Williamson surface roughness model is applied to an ideal surface of pyramids of varying heights.

*4.1. Description of the Greenwood-Williamson model*

The Greenwood and Williamson model (Greenwood and Williamson, 1966; Greenwood and Tripp, 1967) is a widely used surface roughness model which assumes that a rough surface is made up of spherical asperities of radius of curvature $R$, and with tip heights that follow a probability

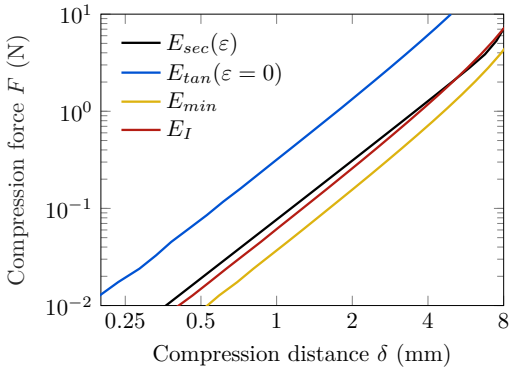


Figure 10: Comparison of the analytic slices model for different prefactors, using the strain dependent modulus $E_{sec}(\varepsilon)$, the small strain tangent modulus $E_{tan}(\varepsilon = 0)$, the minimum of the secant modulus $E_{min}$, and the secant modulus at the inflection point $E_I$.

density function $\phi(z)$. The stiffness of the spherical asperities is based on the mechanics of sphere-to-plane contact (Hertz, 1881), valid for linear elasticity in small deformation, for a size of the contact region and an overlap between bodies much smaller than the dimensions of the bodies themselves, for spherical shapes, and by neglecting contact surface friction and adhesion. The medium is assumed to be isotropic and bulk behavior is neglected, since each asperity behaves independently of the others. Strain hardening, yielding, and thermal effects are neglected.

Asperity height distribution $\phi(z)$ often follows a Gaussian distribution in practice (Bickel, 1963; Greenwood and Tripp, 1967), though any probability density function can be used. Furthermore, the Greenwood-Williamson model uses spherical asperities, though asperities can be of different shapes, as in (Hisakado, 1974; Bush et al., 1975; Persson et al., 2004) for example. Ultimately, the Greenwood-Williamson model predicts the load $F$ required to compress a rough surface with a rigid plane by an amount $\delta$ as

$$F(\delta) = N\frac{4}{3}R^{\frac{1}{2}}E^* \int_{-\infty}^{\delta} (z-\delta)^{\frac{3}{2}}\phi(z)dz, \tag{9}$$

where $N$ is the total number of asperities on the rough surface. The Greenwood-Williamson model considers hemispherical asperities, which gives a prefactor $\frac{4}{3}R^{\frac{1}{2}}E^*$ and a force that increases as $\delta^{\frac{3}{2}}$. These can be changed for pyramidal asperities, using Equation 6, to obtain

$$F(\delta) = N\frac{4}{\pi\sqrt{\pi}}\frac{E^*}{\tan\theta} \int_{-\infty}^{\delta} (z-\delta)^2\phi(z)dz. \tag{10}$$

In this case the prefactor is $\frac{4}{\pi\sqrt{\pi}}\frac{E^*}{\tan\theta}$ and the force increases as $\delta^2$. The sketch of the surface

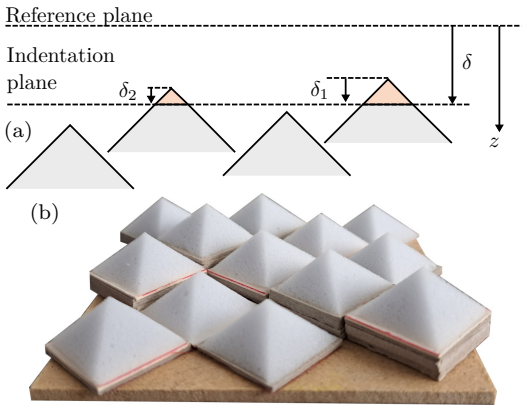


Figure 11: Rough surface represented by pyramidal asperities coming into contact with a rigid plane. (a) Greenwood-Williamson surface roughness model representation. (b) Experimental setup representing a rough surface made up of pyramidal asperities of varying heights.

roughness model composed of pyramids and the corresponding experiment are shown in Figure 11.

### *4.2. Application to a surface of multiple pyramids*

The Greenwood-Williamson model is usually applied to statistically distributed asperities, although it will be used on a surface with a discrete number of asperities for validation. This results in summing the forces of the pyramidal asperities. A surface of 13 pyramidal asperities is created, each with a different height, as shown in Figure 11(b). The pyramids are placed on supports to obtain different heights, and the height of each pyramid is measured individually.

The asperity tip heights are uniformly distributed over a range of 6 mm, meaning that the average height difference between two neighboring pyramid tips is 0.5 mm for 13 pyramids. A uniform distribution was chosen because, compared to a normal distribution for example, it is more feasible to create experimentally and allows for more accurate control over the asperity heights relative to each other. The pyramids are compressed by up to 8.7 mm from the position of the highest pyramid, such that it is compressed by 83.6 % of its initial height. The reference plane is chosen at the tip of the tallest pyramid, which means that the tallest pyramid is expected to contribute to the force quadratically with the total compression distance. A single set of pyramids is characterized this way, considering the averaging effect of compressing 13 pyramids at once and the good measurement repeatability found for single pyramids.

The compression force and the displacement of the indenting plate are measured and compared to predictions in Figure 12. It can be seen that the force resulting from the compression of several pyramids of different heights diverges from the quadratic slope which represents the behavior of a single pyramid. The reaction force is also predicted by using the experimental force and

displacement relationship from Figure 7(a). This relationship provides a robust prediction of the compression force of the multi-asperity surface, from small to large deformations. The analytic result is obtained by applying the modulus of $E = 60.2$ kPa, found experimentally in Section 3.5.3, to Equation 6. The analytic solution converges to the prediction from the experimental force and displacement relationship, because of the good fit it provides for a single pyramid. For very large compression distances $\delta > 7.5$ mm, the analytic model does not predict the force increase found experimentally caused by the finite size of the pyramids, which was already observed for a single pyramid in Section 3.5.3. Overall, the models are able to predict the tendency of the multi-asperity surface, which differs from the quadratic tendency which represents the reaction force of a single asperity.

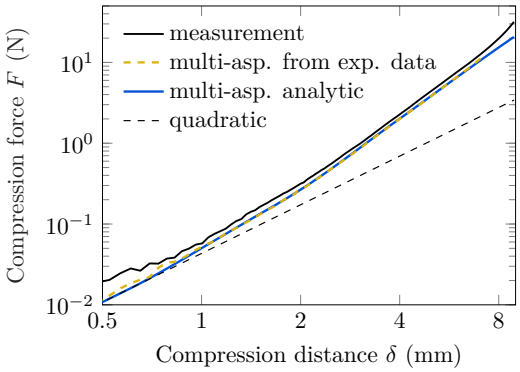


Figure 12: Compression force and compression distance relationship for an ideal surface of 13 pyramids of different heights. Experimental results and predictions using a Greenwood-Williamson like multi-asperity description are plotted. The quadratic tendency expected for a single pyramid is also represented.

In short, extrapolating the behavior of a single pyramid to a surface of several pyramids of varying heights is reliable to predict the compression stiffness of this surface. This prediction is performed on a surface with a finite number of asperities, and can be extended equivalently to a continuous distribution of asperities as described by the Greenwood-Williamson model. This is promising for predicting the compression stiffness of a rough porous material characterized statistically by a 3D surface scan, for example. The ideal surface of pyramids studied is composed solely of asperities, so the transition to the bulk stiffness of the material underneath the asperities does not appear, though this would be the case for a real material undergoing large compression distances relative to the asperity size.

## 5. Conclusion and perspectives

The mechanical behavior of pyramidal asperities made of melamine foam has been studied. It has been shown that material nonlinearity and relaxation can be accounted for to predict the compression stiffness of a multi-pyramidal surface of a cellular material.

First, the nonlinearity of the melamine foam has been observed and can be accounted for with a hyperelastic (hyperfoam) model. Second, the material relaxation can be neglected when the strain rate is high enough, which can be verified with an aging relaxation model that predicts the material's relaxation time.

The effect of the pyramidal geometry has been studied using models of varying complexity. The hyperfoam FEM model and the analytic hyperfoam model, which take account for the material's nonlinear stress-strain relationship, find a quadratic tendency between force and compression distance, which is coherent with experimental results and Kelvin cell FEM simulations. The correlation between the prediction from a continuous model and measurements are satisfactory over several orders of magnitude, except for very small strains, typically below a few tens of cells in contact, and very large strains, typically above 90 % of the total pyramid height. Overall, the combination of the material hyperelasticity with the pyramidal shape nonlinearity results in a quadratic evolution of the force with the compression distance, related to the pyramidal shape. Nevertheless, the material hyperelasticity determines the prefactor of this quadratic tendency, which can be approximated by an average constant value given by the secant modulus evaluated at the inflection point marking the transition from buckling to densification. Finally, the proposed surface roughness model has shown good agreement with experimental results considering an ideal multi-pyramidal material.

Perspectives of this work include exploring incrementally the behavior of different asperity geometries, such as spherical geometries for example, and different asperity height distributions, to generalize the results to different configurations. Furthermore, applying the Greenwood-Williamson surface roughness model to a statistically defined porous material, such as the material pictured in Figure 1(c), would extend these results to real material configurations. Finally, the effect of relaxation on the dynamic behavior of porous materials at long time scales would improve their modelling for vibroacoustic applications.

## Declaration of competing interests

The authors declare that they have no known competing financial interests or personal relationships that could have appeared to influence the work reported in this paper.

## Acknowledgements

This work was supported by Bpifrance through the SEMPAE AAP20 PSPC project. The authors thank collaborators at Trèves Group and Renault Group for discussions. The authors are also grateful to Thomas Boutin for helping in the preparation of the pyramidal samples.

## Declaration on data and code availability

Raw data and computer codes are available from the corresponding author on reasonable request.

## Appendix A. Material relaxation model

It is concluded from experimental compression results in Section 2.3 that the melamine material's response is considered instantaneous when the strain rate is high enough. The objective of this section is to verify this conclusion by modeling the material's relaxation.

### *Appendix A.1. Observation of the relaxation*

When a cylindrical foam sample is subjected to compression at a constant strain, its reaction force drops over time, as visualized in Figure A.13(a). For samples compressed to 30 % strain, the measured force drops by 14.1 % after 1 minute, 20.0 % after 5 minutes, and 40.0 % after 24 hours. The typical relaxation time of the material $\tau = -F/\dot{F}$ in the relaxation phase, shown in Figure A.13(c)-(e), differs noticeably from common viscoelastic models. Despite an apparent convergence of the time response of the compressed sample to its asymptotic behavior after one minute of measurement in Figure A.13(a), it does not in fact reveal an asymptotic limit when observed over an entire day in Figure A.13(b). The observed behavior does not reveal a classical exponential decay as a function time, $F(t) \propto \mathrm{e}^{-t/\tau}$, but instead a power law $F(t) \propto t^n$ with some exponent $n$, as shown in Figure A.13(b). Moreover, it has been found that a viscoelastic Prony series model for foams can sometimes fail to describe their very short-term phenomena (Dalisay et al., 2022). This makes it more difficult to assert whether the material's relaxation time is high enough for its response to be considered instantaneous during a compression ramp.

### *Appendix A.2. Creation of an adapted relaxation model*

Stress relaxation is usually represented using a viscoelastic model. A review of several usual viscoelastic models can be found in (Tschoegl, 1989; Findley et al., 1976). The commonly generalized Maxwell model (Wiechert, 1889, 1893) is represented by a spring placed in parallel with arrangements of springs and dashpots in series. Each spring and dashpot arrangement relaxes over time, resulting in a material that exhibits several decay times. This viscous behavior can be combined with a nonlinear hyperelastic model, and several models have been suggested in the literature. Some authors consider the total stress as the sum of a viscous stress and a hyperelastic stress (Yang and Shim, 2004; Ju et al., 2015), whereas others combine the two into a rheological model (Anani and Alizadeh, 2011; Briody et al., 2012). The material nonlinearity is either represented using a hyperelastic model (Markert, 2005; Briody et al., 2012; Henriques et al., 2020; Dalisay et al., 2022) or a polynomial (Batt et al., 2015) model. The relaxation is either represented

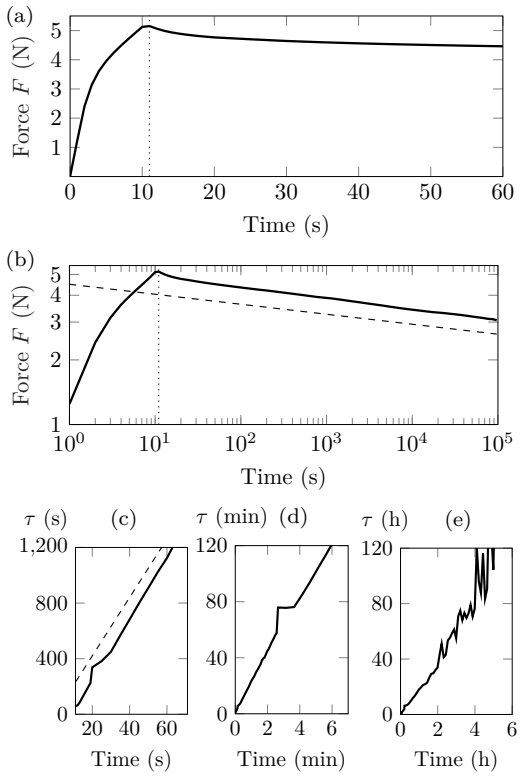


Figure A.13: Stress relaxation of a compressed cylindrical melamine sample at 30 % strain during (a) the first minute and (b) 26 hours. The vertical dashed-dotted line indicates when the stress relaxation at constant strain begins. The relaxation time $\tau = -F/\dot{F}$ increases linearly with time with a constant slope $a = \dot{\tau}$ at (c) early, (d) intermediate, and (e) long-terms. The dashed guideline in (c), $\tau = at$ with arbitrary $a = 21$, relies on a power law dependency, $F(t) \propto t^{-1/a}$, see the dashed guideline in (b).

on the basis of the generalized Maxwell model (Batt et al., 2015; Markert, 2005; Briody et al., 2012), the fractional derivative model (Henriques et al., 2020) or an empirical time-shift method (Grasley and Lange, 2007).

Nevertheless, the continuously varying and linearly increasing relaxation time, $\tau \propto t$, observed in Figure A.13(c)-(e), is characteristic of an aging mechanism (Struik, 1977). The main concern with such mechanisms is determining the dynamics at short times, during which the material is fresh and highly reactive, that is to say $\tau \sim 0$ when $t \sim 0$. For instance, the aging model described by Derec et al. (2001) relates the stress rate $\dot{T}_L$ to the strain rate $\dot{\varepsilon}$ through a history-dependent fluidity term $f$. Espíndola et al. (2012) suggest a simplified expression of the fluidity $f$ resulting in

$$\begin{cases} \dot{T}_L = -fT_L + E\dot{\varepsilon} \\ \dot{f} = -af^2 + r\dot{\varepsilon}^2, \end{cases} \tag{A.1}$$

where $E$ is an elastic modulus, $a$ is a parameter representing material aging (decrease in $f$, *i.e.*

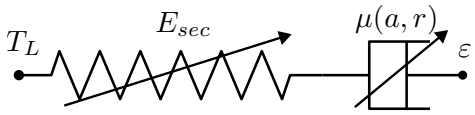


Figure A.14: Schematic representation of the aging model. The nonlinear dashpot represents the nonlinear time dependence of the aging model, and the nonlinear spring represents the hyperelastic response of the material.

increase in relaxation time over time) and $r$ is a parameter representing material rej8uvenation (increase in $f$, *i.e.* decrease of relaxation time over time).

In the case where $f = {}^{E}/_{\mu} = \text{const}$, this model is equivalent to a Maxwell viscoelastic model with a constant relaxation time, where $\mu$ stands for the viscosity of its dashpot. The second line of Equation A.1 indicates the evolution equation of the history dependent fluidity $f$, which is the inverse of a relaxation time: $\tau = \frac{1}{f}$. When the strain rate $\dot{\varepsilon}$ is null, the relaxation time increases linearly with time as $\tau \propto at$, proportionally to the aging parameter $a$, in close agreement with our observations shown in Figure A.13(c)-(e). When the material is being deformed, that is to say $\dot{\varepsilon} \neq 0$, the relaxation time decreases according to rejuvenation parameter $r$, such that $f$ increases and $\tau$ decreases consequently with time.

Considering the fact that the foam response is hyperelastic, we propose an enriched description that encompasses both the hyperelastic and aging behaviors, in which the linear elastic modulus $E$ in Equation A.1 is replaced with the strain-dependent secant modulus $E_{sec}$, as sketched in Figure A.14. This results in a hyperelastic aging model that can fully describe the melamine material's behavior.

*Appendix A.3. Prediction of the full nonlinear and time-dependent material behavior*

The aging hyperelastic model described by Equation A.1 is applied to the melamine foam, and its parameters are determined from experimental data. First, the parameter $a$ is obtained when the strain rate $\dot{\varepsilon}$ is null, in which case $a$ is computed as the slope of $\frac{-T_L}{\dot{T}_L}$. Second, the hyperfoam parameters are obtained from a least squares fit on the instantaneous response of the material. Thus, the parameters ($\alpha_1$, $\mu_1$, $\nu_1$) are obtained from the experimental stress-strain curve between 0 % and 80 % strain performed for a 26 s long ramp, shown in Figure 4. Third, the remaining parameter $r$ is found from compression ramps with different strain rates, as those shown in Figure 4. Compression ramps with strain rates from 3.0 $\%\,\mathrm{s}^{-1}$ to $3.7 \times 10^{-3}$ $\%\,\mathrm{s}^{-1}$ were used to fit the parameter $r$. The parameters obtained for the hyperelastic aging model are presented in Table A.3. It is interesting to note that the Poisson ratio found is close to 0, suggesting that

Table A.3: Parameter values obtained for the hyperelastic aging model used to represent the studied material's behavior, averaged over several measurements, with their standard deviation.

| Hyperfoam parameters | | | Aging parameters | |
|---|---|---|---|---|
| $\alpha_1$ (-) | $\mu_1$ (kPa) | $\nu_1$ (-) | $a$ | $r$ |
| 104.8 | 122.8 | 0.020 | 17.8 | 3.4 |
| $\pm$ 18.5 | $\pm$ 24.5 | $\pm$ 0.005 | $\pm$ 3.6 | $\pm$ 1.7 |

the overall Poisson effect is small, which is a result which can be found in the literature for foams undergoing large strains (Rinde, 1970; Yang and Shim, 2004; Schiffer et al., 2018).

The predictions from the hyperelastic aging model are compared to a measurement in Figure A.15, for the fastest ramp lasting 26 s. The strain ramp over time is shown in Figure A.15(a), and the measured stress is shown in Figure A.15(c), which displays a nonlinear behavior during the loading and stress relaxation when the strain is held constant. The predicted stress response, also shown in Figure A.15(c), exhibits a similar behavior to the measured response. Notably, both the nonlinear behavior and the time-dependent relaxation of the material are captured by the proposed hyperelastic aging model.

The instantaneous stress response of the aging hyperelastic model is shown next to its time-dependent response, which reveals that the time-dependent response is quite close to the instantaneous response for this 26 s compression ramp. Indeed, it can be seen in Figure A.15(b) that the shortest mechanical relaxation time (the inverse of the fluidity $f$) of the material during the 26 s compression ramp is around $\tau = 103.8$ s, indicating that the material relaxation has a weak effect during the compression phase. As a consequence, material relaxation can be safely neglected when the strain rate is large enough, which is the case for this 3.0 % $s^{-1}$ strain ramp, confirming experimental results found in Figure 4.

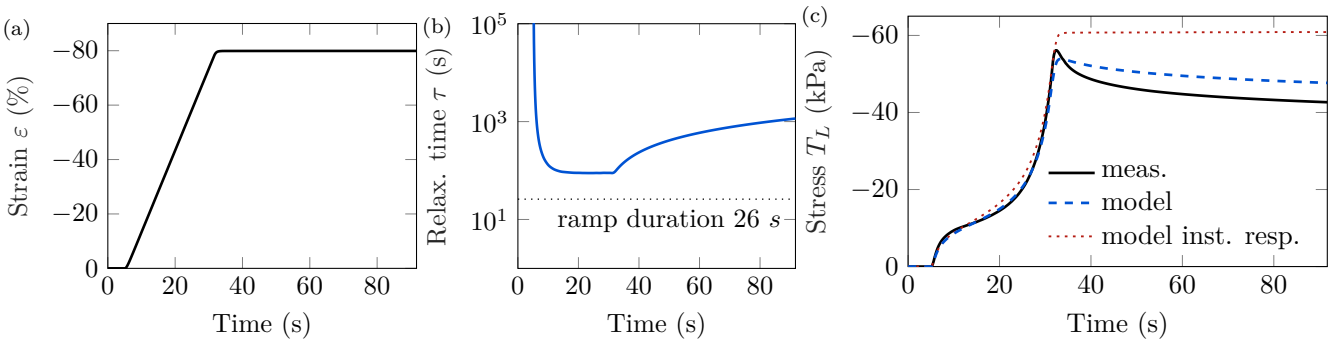


Figure A.15: Comparison of the aging model with measurements for a compression ramp of 0 % to 80 % strain over 26 seconds. (a) Strain applied over time. (b) Predicted material relaxation time $\tau = f^{-1}$ over time, compared with the characteristic time of the compression ramp. (c) Measured stress over time, compared with the predicted stress over time using the hyperelastic aging model. Average parameters from Table A.3 are used, except for $r = 2.49$ which is obtained from a 26 s ramp measurement.

## References


Abaqus Inc., 2006a. Abaqus documentation version 6.6-1: Fitting of hyperelastic and hyperfoam constants. URL: https://classes.engineering.wustl.edu/2009/spring/mase5513/abaqus/docs/v6.6/books/stm/default.htm?startat=ch04s06ath124.html.

Abaqus Inc., 2006b. Abaqus documentation version 6.6-1: Hyperelastic behavior in elastomeric foams. URL: https://classes.engineering.wustl.edu/2009/spring/mase5513/abaqus/docs/v6.6/books/key/default.htm?startat=ch08abk07.html{#}usb-kws-mhyperfoam.

Amédin, C.K., Berry, A., Champoux, Y., 1995. Sound field of a baffled piston source covered by a porous medium layer. J Acoust Soc Am 1766, 1757–1766. URL: https://doi.org/10.1121/1.413440, doi:https://doi.org/10.1121/1.413440.

Anani, Y., Alizadeh, Y., 2011. Visco-hyperelastic constitutive law for modeling of foam's behavior. Mater. Des. 32, 2940–2948. URL: http://dx.doi.org/10.1016/j.matdes.2010.11.010, doi:10.1016/j.matdes.2010.11.010.

Antunes, J.M., Menezes, L.F., Fernandes, J.V., 2006. Three-dimensional numerical simulation of Vickers indentation tests. Int. J. Solids Struct. 43, 784–806. doi:10.1016/j.ijsolstr.2005.02.048.

Ashby, M.F., 1983. Mechanical Properties of Cellular Solids. Metall. Trans. A, Phys. Metall. Mater. Sci. 14 A, 1755–1769. doi:10.1007/BF02645546.

ASTM International, 2001. D 575-91 - Standard Test Methods for Rubber Properties in Compression.

ASTM International, 2002. D 3574-03 - Standard Test Methods for Flexible Cellular Materials - Slab, Bonded, and Molded Urethane Foams.

Batt, G.S., Gibert, J.M., Daqaq, M., 2015. Small strain vibration of a continuous, linearized viscoelastic rod of expanded polymer cushion material. J. Sound Vib. 349, 330–347. URL: http://dx.doi.org/10.1016/j.jsv.2015.03.039, doi:10.1016/j.jsv.2015.03.039.

Belingardi, G., Montanini, R., Avalle, M., 2001. Characterization of polymeric structural foams under compressive impact loading by means of energy-absorption diagram. Int. J. Impact Eng. 25, 455–472.

Bickel, E., 1963. Some Fundamental Problems in the Measurement of Surface Roughness, in: Proc. Int. Prod. Eng. Res. Conf., Pittsburgh, Pa.. pp. 667–674.

Bolton, J.S., Shiau, N.M., Kang, Y.J., 1996. Sound transmission through multi-panel structures lined with elastic porous materials. J. Sound Vib. 191, 317–347. doi:10.1006/jsvi.1996.0125.

Bonfiglio, P., Pompoli, F., Horoshenkov, K.V., Rahim, M.I.B.A., Jaouen, L., Rodenas, J., Bécot, F.X., Gourdon, E., Jaeger, D., Kursch, V., Tarello, M., Roozen, N.B., Glorieux, C., Ferrian, F., Leroy, P., Vangosa, F.B., Dauchez, N., Foucart, F., Lei, L., Carillo, K., Doutres, O., Sgard, F., Panneton, R., Verdiere, K., Bertolini, C., Bär, R., Groby, J.P., Geslain, A., Poulain, N., Rouleau, L., Guinault, A., Ahmadi, H., Forge, C., 2018. How reproducible are methods to measure the dynamic viscoelastic properties of poroelastic media? J. Sound Vib. 428, 26–43. doi:10.1016/j.jsv.2018.05.006.

Briody, C., Duignan, B., Jerrams, S., Tiernan, J., 2012. The implementation of a visco-hyperelastic numerical material model for simulating the behaviour of polymer foam materials. Comput. Mater. Sci. 64, 47–51. URL: http://dx.doi.org/10.1016/j.commatsci.2012.04.012, doi:10.1016/j.commatsci.2012.04.012.

Bush, A.W., Gibson, R.D., Thomas, T.R., 1975. The elastic contact of a rough surface. Wear 35, 87–111. doi:10.1016/0043-1648(75)90145-3.

Campolina, B., Dauchez, N., Atalla, N., Doutres, O., 2012. Effect of porous material compression on the sound transmission of a covered single leaf panel. Appl. Acoust. 73, 791–797. doi:https://doi.org/10.1016/j.apacoust.2012.02.013.

Cavender, K.D., Kinkelaar, M.R., 1996. Real time dynamic comfort and performance factors of polyurethane foam in automotive seating. SAE Tech. Pap. , 18doi:10.4271/960509.

Chen, J.S., Sun, C.T., 2012. Reducing vibration of sandwich structures using antiresonance frequencies. Compos. Struct. 94, 2819–2826. URL: http://dx.doi.org/10.1016/j.compstruct.2012.03.041, doi:10.1016/j.compstruct.2012.03.041.

Chevillotte, F., Ronzio, F., Bertolini, C., Hoang, M.T., Dejaeger, L., Lei, L., Duval, A., Mordillat, P., 2020. Inter-Laboratory Characterization of Biot Parameters of Poro-Elastic Materials for Automotive Applications. SAE Tech. Pap. , 1–9doi:10.4271/2020-01-1523.

Cummings, A., Rice, H.J., Wilson, R., 1999. Radiation damping in plates, induced by porous media. J. Sound Vib. 221, 143–167. doi:10.1006/jsvi.1998.1987.

Dalisay, J.D.E., Liu, L., Eriten, M., Bergman, L.A., Vakakis, A.F., 2022. Characterization of visco-hyperelastic behavior of open cell polyurethane foam through transient shear testing. Int. J. Solids Struct. 241, 111482. URL: https://doi.org/10.1016/j.ijsolstr.2022.111482, doi:10.1016/j.ijsolstr.2022.111482.

Dauchez, N., 2014. Effect of static preload on Young modulus, in: SAPEM 2014, Stockholm, Sweden. pp. 1–13. URL: https://sapem2014.matelys.com/.

Dauchez, N., Etchessahar, M., Sahraoui, S., 2002. On measurement of mechanical properties of sound absorbing materials, in: 2nd Biot Conf. poromechanics, pp. 1–4. URL: http://hal.archives-ouvertes.fr/hal-00331372/.

Derec, C., Ajdari, A., Lequeux, F., 2001. Rheology and aging: A simple approach. Eur. Phys. J. E 4, 355–361. doi:10.1007/s101890170118.

Doutres, O., Atalla, N., Dong, K., 2011. Effect of the microstructure closed pore content on the acoustic behavior of polyurethane foams. J. Appl. Phys. 110. doi:10.1063/1.3631021.

Doutres, O., Dauchez, N., Génevaux, J.M., 2007. Porous layer impedance applied to a moving wall: Application to the radiation of a covered piston. J. Acoust. Soc. Am. 121, 206–213. doi:10.1121/1.2359233.

Espíndola, D., Galaz, B., Melo, F., 2012. Ultrasound induces aging in granular materials. Phys. Rev. Lett. 109. doi:10.1103/PhysRevLett.109.158301.

Findley, W.N., Lai, J.S., Onaran, K., Christensen, R.M., 1976. Creep and Relaxation of Nonlinear Viscoelastic Materials With an Introduction to Linear Viscoelasticity. Dover publications, inc., New York. doi:10.1115/1.3424077.

Ge, C., Rice, B., 2018. Impact damping ratio of a nonlinear viscoelastic foam. Polym. Test. 72, 187–195. URL: https://doi.org/10.1016/j.polymertesting.2018.10.023, doi:10.1016/j.polymertesting.2018.10.023.

Geslain, A., Dazel, O., Groby, J.P., Sahraoui, S., Lauriks, W., 2011. Influence of static compression on mechanical parameters of acoustic foams. J. Acoust. Soc. Am. 130, 818–825. doi:10.1121/1.3605535.

Gibson, L.J., 1989. Modelling the mechanical behavior of cellular materials. Mater. Sci. Eng. A 110, 1–36. doi:10.1016/0921-5093(89)90154-8.

Gibson, L.J., Ashby F, 1997. Cellular Solids: Structure and Properties. 2nd editio ed., Cambridge University Press, Cambridge. URL: https://doi.org/10.1017/CBO9781139878326, doi:10.1017/CBO9781139878326.

Gong, L., Kyriakides, S., Triantafyllidis, N., 2005. On the stability of Kelvin cell foams under compressive loads. J. Mech. Phys. Solids 53, 771–794. doi:10.1016/j.jmps.2004.10.007.

Grasley, Z.C., Lange, D.A., 2007. Constitutive modeling of the aging viscoelastic properties of portland cement paste. Mech. Time-Dependent Mater. 11, 175–198. doi:10.1007/s11043-007-9043-4.

Greenwood, J.A., Tripp, J.H., 1967. The elastic contact of rough spheres. J. Appl. Mech. Trans. ASME 34, 153–159. doi:10.1115/1.3607616.

Greenwood, J.A., Williamson, J.B.P., 1966. Contact of nominally flat surfaces. Proc. R. Soc. Lond. A. 295, 300–319. doi:10.1098/rspa.1966.0242.

Guastavino, R., Göransson, P., 2007. A 3D displacement measurement methodology for anisotropic porous cellular foam materials. Polym. Test. 26, 711–719. doi:10.1016/j.polymertesting.2007.02.008.

Henriques, I.R., Rouleau, L., Castello, D.A., Borges, L.A., Deü, J.F., 2020. Viscoelastic behavior of polymeric foams: Experiments and modeling. Mech. Mater. 148. doi:10.1016/j.mechmat.2020.103506.

Hentati, C., Job, S., Crété, J.P., Taktak, M., Haddar, M., Dauchez, N., 2020. On the contact law of open-cell poro-granular materials. Int. J. Solids Struct. 208-209, 83–92. URL: https://doi.org/10.1016/j.ijsolstr.2020.10.023, doi:10.1016/j.ijsolstr.2020.10.023.

Hertz, H., 1881. On the contact of elastic solids. J. für die reine und Angew. Math. 92, 156–171.

Hill, R., 1979. Aspects of Invariance in Solid Mechanics. volume 18. doi:10.1016/S0065-2156(08)70264-3.

Hisakado, T., 1974. Effect of surface roughness on contact between solid surfaces. Wear 28, 217–234. doi:10.1016/0043-1648(74)90163-X.

Hoang, M.T., 2012. Modélisation et simulation multi-échelle et multi-physique du comportement acoustique de milieux poroélastiques : application aux mousses de faible densité. Ph.D. thesis. Universite Paris-Est. URL: https://theses.hal.science/tel-00799779v3.

Jaouen, L., Renault, A., Deverge, M., 2008. Elastic and damping characterizations of acoustical porous materials: Available experimental methods and applications to a melamine foam. Appl. Acoust. 69, 1129–1140. doi:10.1016/j.apacoust.2007.11.008.

Ju, M.L., Jmal, H., Dupuis, R., Aubry, E., 2015. Visco-hyperelastic constitutive model for modeling the quasi-static behavior of polyurethane foam in large deformation. Polym. Eng. Sci. 55, 1795–1804. doi:10.1002/pen.24018.

King, R.B., 1987. Elastic analysis of some punch problems for a layered medium. Int. J. Solids Struct. 23, 1657–1664. URL: http://dx.doi.org/10.1016/0020-7683(87)90116-8, doi:10.1016/0020-7683(87)90116-8.

Kino, N., Ueno, T., 2008. Comparisons between characteristic lengths and fibre equivalent diameters in glass fibre and melamine foam materials of similar flow resistivity. Appl. Acoust. 69, 325–331. doi:10.1016/j.apacoust.2006.11.008.

Lagarrigue, C., Groby, J.P., Tournat, V., Dazel, O., Umnova, O., 2013. Absorption of sound by porous layers with embedded periodic arrays of resonant inclusions. J. Acoust. Soc. Am. 134, 4670–4680. doi:10.1121/1.4824843.

Lee, H.M., Kim, D.H., Kim, D.Y., Kim, M.S., Park, J., Yoon, G.H., 2022. Enhancement of vibration attenuation and shock absorption in composite sandwich structures with porous foams and surface patterns. Compos. Struct. 295, 115755. URL: https://doi.org/10.1016/j.compstruct.2022.115755, doi:10.1016/j.compstruct.2022.115755.

Lei, L., 2018. Étude des matériaux poreux thermocompressés pour la modélisation des écrans acoustiques automobiles. Ph.D. thesis. Laboratoire Roberval, Université de technologie de Compiègne.

Li, Q.M., Magkiriadis, I., Harrigan, J.J., 2006. Compressive strain at the onset of densification of cellular solids. J. Cell. Plast. 42, 371–392. doi:10.1177/0021955X06063519.

Luo, S., Huang, Q., 2014. Resonance variation of double-layer structure composed of porous material and air layer based on biot theory. Acta Acust. united with Acust. 100, 477–484. doi:10.3813/AAA.918728.

Mao, H., Rumpler, R., Göransson, P., 2021. A note on the linear deformations close to the boundaries of a cellular material. Mech. Res. Commun. 111. doi:10.1016/j.mechrescom.2021.103657.

Markert, B., 2005. Porous media viscoelasticity with application to polymeric foams. Ph.D. thesis. Universität Stuttgart. URL: http://elib.uni-stuttgart.de/opus/volltexte/2005/2338/.

Mooney, M., 1940. A theory of large elastic deformation. J. Appl. Phys. 11, 582–592. doi:10.1063/1.1712836.

Novak, R.A., 1992. Sound insulation of lightweight double walls. Appl. Acoust. 37, 281–303. doi:10.1016/0003-682X(92)90016-L.

Ogden, R.W., 1972. Large Deformation Isotropic Elasticity - on the Correlation of Theory and Experiment for Incompressible Rubberlike Solids, in: Proc. R. Soc. Long. A., pp. 565–584. doi:10.5254/1.3542910.

Oh, J.H., Kim, J.S., Nguyen, V.H., Oh, I.K., 2020. Auxetic graphene oxide-porous foam for acoustic wave and shock energy dissipation. Compos. Part B Eng. 186, 107817. URL: https://doi.org/10.1016/j.compositesb.2020.107817, doi:10.1016/j.compositesb.2020.107817.

Panneton, R., Atalla, N., 1996. Numerical prediction of sound transmission through finite multilayer systems with poroelastic materials. J. Acoust. Soc. Am. 100, 346–354. doi:10.1121/1.415956.

Persson, B.N., Albohr, O., Tartaglino, U., Volokitin, A.I., Tosatti, E., 2004. On the nature of surface roughness with application to contact mechanics, sealing, rubber friction and adhesion. J. Phys. Condens. Matter 17, 0–62. doi:10.1088/0953-8984/17/1/R01.

Renault, 2014. D41 1003 - Matériaux alvérolaires souples de garnissage - Résistance à la compression (portance).

Rinde, J.A., 1970. Poisson's Ratio for Rigid Plastic Foams. J. Appl. Polym. Sci. 14, 1913–1926.

Rivlin, R.S., Saunders, D.W., Rivlin, B.Y.R.S., 1951. large elastic deformations of isotropic materials VII . Experiments on the deformation of rubbBritish Rubber Producers' Research Association. Philos. Trans. R. Soc. 243, 251–288. doi:https://doi.org/10.1098/rsta.1951.0004.

R.S.Rivlin, 1947. Large elastic deformations of isotropic materials. I. Fundamental concepts. Br. Rubber Prod. Res. Assoc. , 459–490.

Schiffer, A., Lee, D., Kim, E., Kim, T.Y., 2018. Interaction of highly nonlinear solitary waves with rigid polyurethane foams. Int. J. Solids Struct. 152-153, 39–50. doi:10.1016/j.ijsolstr.2018.05.010.

Sirghi, L., Ponti, J., Broggi, F., Rossi, F., 2008. Probing elasticity and adhesion of live cells by atomic force microscopy indentation. Eur. Biophys. J. 37, 935–945. doi:10.1007/s00249-008-0311-2.

Sneddon, I.N., 1965. The relation between load and penetration in the axisymmetric boussinesq problem for a punch of arbitrary profile. Int. J. Eng. Sci. 3, 47–57. doi:10.1016/0020-7225(65)90019-4.

Storåkers, B., 1986. On material representation and constitutive branching in finite compressible elasticity. J. Mech. Phys. Solids 34, 125–145. doi:10.1016/0022-5096(86)90033-5.

Struik, L., 1977. Physical aging in amorphous polymers and other materials. Ph.D. thesis. T.U. Delft. URL: http://resolver.tudelft.nl/uuid:941d2af6-903a-4260-9953-2efb4cb38d2e, doi:10.1016/0040-6031(82)85085-5.

Tan, P.J., Harrigan, J.J., Reid, S.R., 2002. Inertia effects in uniaxial dynamic compression of a closed cell aluminium alloy foam. Mater. Sci. Technol. 18, 480–488. doi:10.1179/026708302225002092.

Tan Hoang, M., Perrot, C., 2012. Solid films and transports in cellular foams. J. Appl. Phys. 112. doi:10.1063/1.4751345.

Tschoegl, N.W., 1989. The phenomenological theory of linear viscoelastic behavior. 1st editio ed., Berlin.

Wang, Y., Low, K.H., 2005. Damped response analysis of nonlinear cushion systems by a linearization method. Comput. Struct. 83, 1584–1594. doi:10.1016/j.compstruc.2005.02.004.

White, S.W., Kim, S.K., Bajaj, A.K., Davies, P., Showers, D.K., Liedtke, P.E., 2000. Experimental techniques and identification of nonlinear and viscoelastic properties of flexible polyurethane foam. Nonlinear Dyn. 22, 281–313. doi:10.1023/A:1008302208269.

Wiechert, E., 1889. Ueber elastische Nachwirkung. Hartungsche buchdr. URL: https://books.google.fr/books?id=wCWhAQAACAAJ.

Wiechert, E., 1893. Gesetze der elastischen Nachwirkung für constante Temperatur. Ann. Phys. 286, 335–348. doi:https://doi.org/10.1002/andp.18932861110.

Xing, Y., Sun, D., Zhang, M., Shu, G., 2023. Crushing Responses of Expanded Polypropylene Foam. Polymers (Basel). 15. doi:10.3390/polym15092059.

Yang, F., Li, Z., Liu, Z., Zhuang, Z., 2021. Shock Loading Mitigation Performance and Mechanism of the PE/Wood/PU/Foam Structures. Int. J. Impact Eng. 155, 103904. URL: https://doi.org/10.1016/j.ijimpeng.2021.103904, doi:10.1016/j.ijimpeng.2021.103904.

Yang, L.M., Shim, V.P., 2004. A visco-hyperelastic constitutive description of elastomeric foam. Int. J. Impact Eng. 30, 1099–1110. doi:10.1016/j.ijimpeng.2004.03.011.